

The interplay of large two-magnon ferromagnetic resonance linewidths and low Gilbert damping in Heusler thin films

W. K. Peria,¹ T. A. Peterson,¹ A. P. McFadden,² T. Qu,³ C. Liu,¹ C. J. Palmström,^{2,4} and P. A. Crowell¹

¹*School of Physics and Astronomy, University of Minnesota, Minneapolis, Minnesota 55455*

²*Department of Electrical & Computer Engineering, University of California, Santa Barbara, California 93106*

³*Department of Electrical and Computer Engineering, University of Minnesota, Minneapolis, Minnesota 55455*

⁴*Department of Materials, University of California, Santa Barbara, California 93106*

We report on broadband ferromagnetic resonance linewidth measurements performed on epitaxial Heusler thin films. A large and anisotropic two-magnon scattering linewidth broadening is observed for measurements with the magnetization lying in the film plane, while linewidth measurements with the magnetization saturated perpendicular to the sample plane reveal low Gilbert damping constants of $(1.5 \pm 0.1) \times 10^{-3}$, $(1.8 \pm 0.2) \times 10^{-3}$, and $< 8 \times 10^{-4}$ for $\text{Co}_2\text{MnSi}/\text{MgO}$, $\text{Co}_2\text{MnAl}/\text{MgO}$, and $\text{Co}_2\text{FeAl}/\text{MgO}$, respectively. The in-plane measurements are fit to a model combining Gilbert and two-magnon scattering contributions to the linewidth, revealing a characteristic disorder lengthscale of 10-100 nm.

I. INTRODUCTION

The theoretical understanding of the damping mechanism believed to govern longitudinal magnetization relaxation in metallic ferromagnets, originally due to Kamberský [1, 2], has in recent years resulted in quantitative damping estimates for realistic transition metal band structures [3–5]. Although of great interest where engineering of damping is desired [6], these calculations remain largely uncompered to experimental data. Kamberský damping may be characterized by the so-called Gilbert damping constant α in the Landau-Lifshitz-Gilbert macrospin torque equation of motion, and formally describes how the spin-orbit interaction in itinerant electron systems results in damping of magnetization dynamics [2]. Schoen *et al.* [7] have reported that α is minimized for Co-Fe alloy compositions at which the density-of-states at the Fermi level is minimized, in reasonable agreement with Kamberský model predictions [8]. Furthermore, half-metallic, or near half-metallic ferromagnets such as full-Heusler compounds have been predicted to demonstrate ultralow Kamberský α ($\leq 10^{-3}$) due to their spin-resolved band structure near the Fermi level [9]. Finally, anisotropy of the Kamberský damping in single crystals has been predicted, which is more robust for Fermi surfaces with single-band character [5, 10].

The Gilbert damping constant is often reported through measurements of the ferromagnetic resonance (FMR) linewidth ΔH , which may be expressed as a sum of individual contributions

$$\Delta H = \frac{2\alpha f}{\gamma} + \Delta H_0 + \Delta H_{TMS}, \quad (1)$$

where the first term is the Gilbert damping linewidth (f is the FMR frequency, γ is the gyromagnetic ratio), ΔH_0 is a frequency-independent inhomogeneous broadening, and ΔH_{TMS} represents an extrinsic two-magnon scattering (TMS) linewidth contribution [11, 12] that is, in general, a nonlinear function of frequency. In recent

years it has been realized that TMS linewidths are pervasive for the conventional in-plane geometry of thin film FMR measurements, requiring either the perpendicular-to-plane FMR geometry [13] (for which TMS processes are suppressed) or sufficiently broadband measurements [14] to extract the bare Gilbert α . For instance, recent FMR linewidth studies on Heusler compounds have reported distinct TMS linewidths [15, 16], which challenged simple inference of the Gilbert α .

In this article, we present FMR linewidth measurements for epitaxial Heusler thin films for all principal orientations of the magnetization with respect to the symmetry axes. For the in-plane configuration, large and anisotropic TMS-dominated linewidths are observed. In the perpendicular-to-plane configuration, for which the TMS process is inactive [11], the Gilbert α and inhomogeneous broadening are measured. We find evidence of low ($\sim 10^{-3}$) Gilbert α in these Heusler thin films accompanied by large and anisotropic TMS for in-plane magnetization. We conclude by discussing the interplay of low Gilbert α and large TMS, and emphasize the nature by which the TMS may conceal the presence of anisotropic Kamberský α .

II. SAMPLES

The Heusler alloy films used for these measurements were grown by molecular beam epitaxy (MBE) by co-evaporation of elemental sources in ultrahigh vacuum (UHV). The $\text{MgO}(001)$ substrates were annealed at 700 °C in UHV followed by growth of a 20 nm thick MgO buffer layer by e-beam evaporation at a substrate temperature of 630 °C. The 10 nm thick Co_2MnAl and Co_2MnSi films were grown on the MgO buffer layers at room temperature and then annealed at 600 °C *in situ* in order to improve crystalline order and surface morphology. The 24 nm thick Co_2FeAl sample was grown using the same MgO substrate and buffer layer preparation,

but at a substrate temperature of 250 °C with no post-growth anneal. Reflection high energy electron diffraction (RHEED) was monitored during and after growth of all samples and confirmed the expected epitaxial relationship of MgO(001)⟨110⟩ || Heusler(001)⟨100⟩. X-ray diffraction (XRD) confirmed a single phase of (001)-oriented Co₂FeAl, along with the presence of the (002) reflection confirming B2 or L₂₁ ordering. All of the films were capped with several nm of e-beam evaporated AlOx for passivation prior to atmospheric exposure. The saturation magnetization for the 24 nm thick Co₂FeAl film was determined from anomalous Hall effect saturation field to be 1200 emu/cm³, which is consistent with measurements of Ref. [17] for L₂₁ or B2-ordered films, along with 990 emu/cm³ and 930 emu/cm³ for the Co₂MnSi and Co₂MnAl films, respectively. Hereafter, we will refer to the Co₂MnSi(10 nm)/MgO as the “CMS” film, the Co₂MnAl(10 nm)/MgO film as the “CMA” film, and the Co₂FeAl(24 nm)/MgO film as the “CFA” film.

III. EXPERIMENT

Broadband FMR linewidth measurements were performed at room temperature with a coplanar waveguide (CPW) transmission setup, similar to that discussed in detail in Refs. [18, 19] [see Fig. 1(a)] placed between the pole faces of an electromagnet. A ~mm² cleaved piece of the sample was placed face-down over the centerline of the CPW. A rectifying diode was used to detect the transmitted microwave power, and a ~100 Hz magnetic field modulation was used for lock-in detection of the transmitted power, resulting in a signal $\propto d\chi/dH$ (where χ is the film dynamic magnetic susceptibility). The excitation frequency could be varied from 0-50 GHz, and a microwave power near 0 dBm was typically used. It was verified that all measurements discussed in this article were in the small precession cone angle, linear regime. The orientation of the applied magnetic field could be rotated to arbitrary angle in the film plane (IP), or applied perpendicular to the film plane (PP). We emphasize again that TMS contributions are suppressed in the PP configuration [12]. The resonance fields were fit as a function of applied frequency in order to extract various magnetic properties of the films (anisotropy field, effective magnetizations, etc., see Table I). The magnetic free energy per unit volume used to generate the resonance conditions for these samples is given by

$$F_{\mathbf{M}} = -\mathbf{M} \cdot \mathbf{H} + K_1 \sin^2 \phi \cos^2 \phi + 2\pi M_{eff}^2 \cos^2 \theta \quad (2)$$

where \mathbf{H} is the applied field, ϕ and θ are the azimuthal and polar angles of the magnetization, respectively, K_1 is a first order in-plane cubic anisotropy constant, and $4\pi M_{eff}$ is the PP saturation field which includes the usual demagnetization energy and a first order uniaxial anisotropy due to interfacial effects. The magnetic-field-swept FMR lineshapes were fit to the derivative of

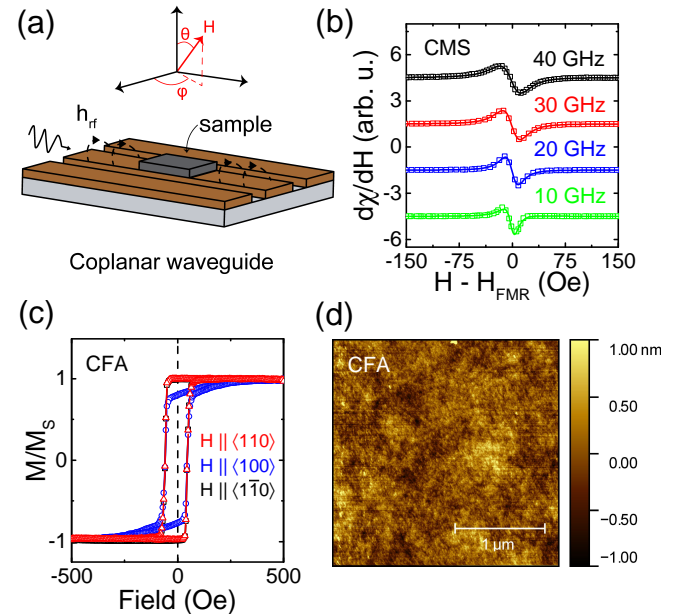


FIG. 1. (a) Field-swept CPW FMR setup used in this experiment. (b) Typical derivative susceptibility lineshapes for these samples at different microwave excitation frequencies. The fits are shown as solid lines. (c) In-plane hysteresis loops for CFA obtained with a vibrating-sample magnetometer (VSM). (d) Atomic force microscopy (AFM) image of surface topography for CFA. RMS roughness is 0.2 nm.

Lorentzian functions [19] in order to extract the full-width at half-maximum linewidths ΔH [magnetic field units, Fig. 1(b)], which are the focus of this article. The maximum resonant frequency was determined by the maximum magnetic field that could be applied for both IP and PP electromagnet configurations, which was 10.6 kOe and 29 kOe, respectively. For the IP measurement, the angle of the applied field in the plane of the film was varied to determine the in-plane magnetocrystalline anisotropy of our samples, which was fourfold-symmetric for the three films characterized in this article (see Fig. 3). The anisotropy was confirmed using vibrating-sample magnetometry (VSM) measurements, an example of which is shown in Fig. 1(c), which shows IP easy and hard axis hysteresis loops for the CFA film. For the PP measurement, alignment was verified to within ~0.1° to ensure magnetization saturation just above the PP anisotropy field, thus minimizing field-dragging contributions to the linewidth.

IV. RESULTS AND ANALYSIS

A. Perpendicular-to-plane linewidths

First we discuss the results of the PP measurement. As stated in Sec. III, the TMS extrinsic broadening mecha-

TABLE I. Summary of the magnetic properties extracted from the dependence of the resonance field on applied frequency for both field in-plane (\parallel) and field perpendicular-to-plane (\perp) configurations, along with the Gilbert α and inhomogeneous broadening from the perpendicular-to-plane configuration. $2K_1/M_s$ and $4\pi M_{eff}^{\parallel}$ are the in-plane and perpendicular-to-plane anisotropy fields, respectively (see Eq. 2), and g is the Landé g -factor.

Sample	$2K_1/M_s$ (Oe)	$4\pi M_{eff}^{\parallel}$ (kOe)	$4\pi M_{eff}^{\perp}$ (kOe)	g^{\parallel}	g^{\perp}	$\alpha_{001} \times 10^{-3}$	ΔH_0 (Oe)
CMS	280	12.3	13.3	2.04	2.04	1.5 ± 0.1	9
CMA	35	11.3	11.7	2.06	2.08	1.8 ± 0.2	12
CFA	230	15.1	15.5	2.06	2.07	< 0.8	100

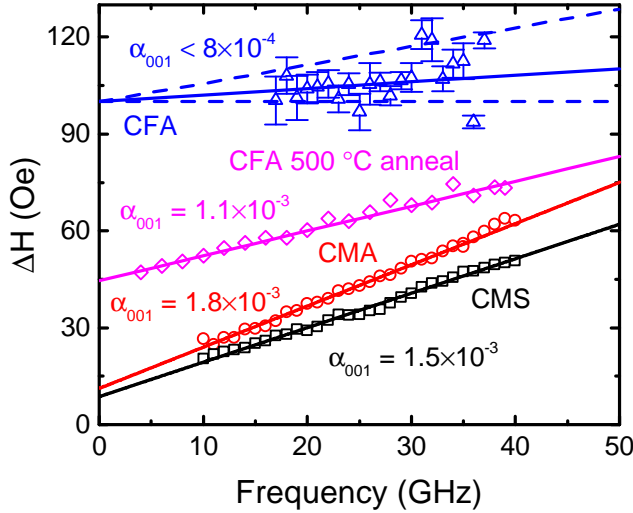


FIG. 2. Linewidths as a function of frequency with the field applied perpendicular to plane, for which two-magnon scattering is inactive. The black squares are data for the CMS film, the red circles are for the CMA film, and the blue triangles are for the CFA film. In addition, linewidths are shown for a CFA film that was annealed at 500 °C *ex situ* (magenta diamonds). Corresponding linear fits are shown along with the extracted Gilbert damping factor α . The blue dashed lines indicate an upper bound of $\alpha_{001} = 8 \times 10^{-4}$ and a lower bound of $\alpha_{001} = 0$ for CFA.

nism is suppressed when the magnetization is normal to the plane of the film. We can thus fit our data to Eq. 1 with $\Delta H_{TMS} = 0$, greatly simplifying the extraction of the Gilbert damping constant α and the inhomogeneous broadening ΔH_0 . Prior knowledge of ΔH_0 is particularly important for constraining the analysis of the IP measurements, as we shall discuss.

The dependence of ΔH on frequency for the CMS, CMA, and CFA films in the PP configuration is summarized in Fig. 2, in which fits to Eq. 1 are shown with ΔH_{TMS} set to zero. For the CMS film, $\alpha_{001} = (1.5 \pm 0.1) \times 10^{-3}$ and $\Delta H_0 = 9$ Oe, while for the CMA film $\alpha_{001} = (1.8 \pm 0.2) \times 10^{-3}$ and $\Delta H_0 = 12$ Oe. $\text{Co}_2\text{MnSi}_{2/3}\text{Al}_{1/3}/\text{MgO}$ and $\text{Co}_2\text{MnSi}_{1/3}\text{Al}_{2/3}/\text{MgO}$ films (both 10 nm thick) were also measured, with Gilbert damping values of $\alpha_{001} = (1.8 \pm 0.2) \times 10^{-3}$ and $\alpha_{001} = (1.5 \pm 0.1) \times 10^{-3}$, re-

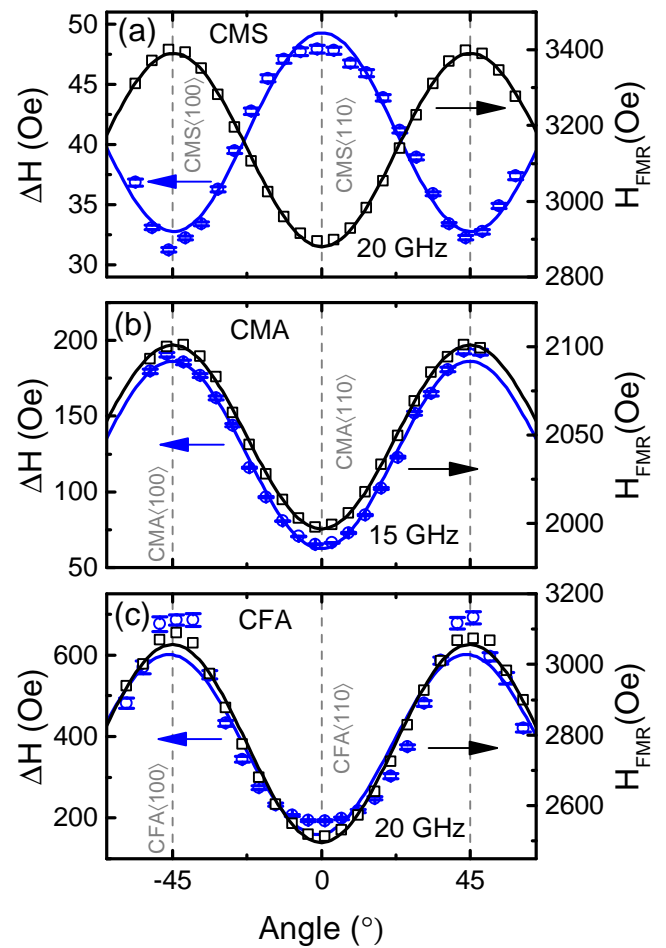


FIG. 3. Azimuthal angular dependence of the linewidths (left ordinate, blue circles) and resonance fields (right ordinate, black squares) for (a) CMS, (b) CMA, and (c) CFA. The excitation frequency was 20 GHz for CMS, 15 GHz for CMA, and 20 GHz for CFA. The solid lines are sinusoidal fits.

spectively (not shown). For CFA, we obtained a damping value of $\alpha_{001} = 3 \times 10^{-4}$ with an upper bound of $\alpha_{001} < 8 \times 10^{-4}$ and $\Delta H_0 = 100$ Oe. The source of the large inhomogeneous broadening for the CFA film is unclear: AFM measurements [Fig. 1(d)] along with XRD indicate that the film is both crystalline and smooth. It is possible that the broadening is related to the co-

existence of ordered L2₁ and disordered B2 phases, but this requires more investigation. Note that the range of frequencies shown in Fig. 2 are largely governed by considerations involving the Kittel equation [20]: measurements below 10 GHz were not used due to the increasing influence of slight misalignment on ΔH (through field-dragging) at FMR conditions just above the PP saturation fields. A piece of the CFA sample was annealed at 500 °C *ex situ*, which reduced the inhomogeneous broadening to ~ 45 Oe (still a relatively large value) and increased the Gilbert damping to $\alpha_{001} = 1.1 \times 10^{-3}$ (similar behavior in CFA was seen in Ref. [21]). The constraint of $\alpha_{001} < 8 \times 10^{-4}$ is among the lowest of reported Gilbert damping constants for metallic ferromagnets, but the $\alpha \sim 10^{-4}$ range is not unexpected based on Kamberský model calculations performed for similar full-Heusler compounds [9] or other recent experimental reports [22, 23]. It should be noted that Schoen *et al.* [7] have recently reported $\alpha = 5 \times 10^{-4}$ for Co₂₅Fe₇₅ thin films, where spin pumping and radiative damping contributions were subtracted from the raw measurement. Spin pumping contributions to the intrinsic damping are not significant in our films, as no heavy-metal seed layers have been used and the films have thicknesses of 10 nm or greater. For the radiative damping contribution [13] in the geometry of our CPW and sample, we calculate contributions $\alpha_{\text{rad}} \lesssim 1 \times 10^{-4}$, which is below the uncertainty in our damping fit parameter.

B. In-plane linewidths

With the intrinsic damping and inhomogeneous broadening characterized by the PP measurement, we turn our attention to the IP linewidth measurements, for which TMS contributions are present. Figure 3 shows the dependences of the resonance fields and linewidths on the angle of the in-plane field. An important observation seen in Fig. 3 is that the linewidth extrema are commensurate with those of the resonance fields and therefore the magnetocrystalline anisotropy energy. This rules out field-dragging and mosaicity effects that can occur when the resonance field depends strongly on angle [24]. Similar IP angular dependence of the FMR linewidth, which was attributed to an anisotropic TMS mechanism caused by a rectangular array of misfit dislocations, has been reported by Kurebayashi *et al.* [25] and Woltersdorf and Heinrich [14] for epitaxial Fe/GaAs(001) ultrathin films.

To further study the anisotropy of the IP ΔH in our films, we have measured ΔH at the angles corresponding to the extrema of H_{FMR} (and ΔH) in Fig. 3 over a range of frequencies. These data are shown in Fig. 4, along with the PP ([001]) measurements for each sample. A distinguishing feature of the data shown in Fig. 4 is the significant deviation between IP and PP linewidths in all but one case (CMS<100>). Large and nonlinear frequency dependence of the IP linewidths is strongly suggestive of an active TMS linewidth broadening mechanism in these

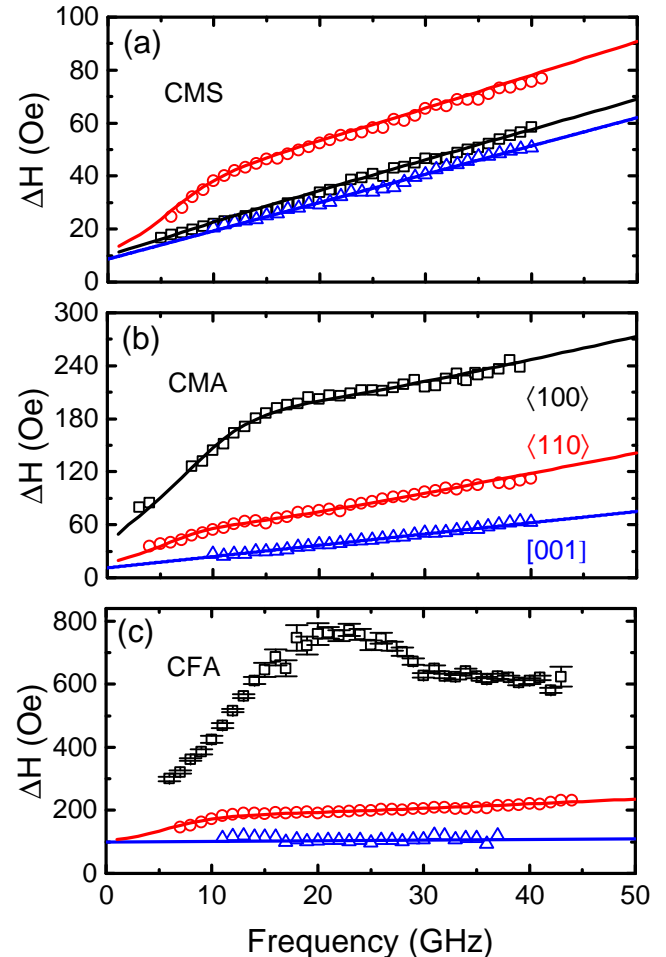


FIG. 4. Linewidths along all three principal directions for CMS (a), CMA (b), and CFA (c). Heusler crystalline axes are labeled by <100> (black), <110> (red), and [001] (blue). In all three cases, <110> is the in-plane easy axis and <100> is the in-plane hard axis. The corresponding fits are shown as the solid curves, where the in-plane linewidths are fit using Eq. 3 and the out-of-plane linewidths are fit to the Gilbert damping model.

films. In the presence of TMS, careful analysis is required to separate Gilbert damping from TMS linewidth contributions. Therefore, in the following section we describe the TMS mechanism in more detail in order to analyze the IP linewidths in Fig. 4 and extract the Gilbert damping.

C. Two-magnon scattering model

The TMS mechanism leads to a characteristic nonlinear frequency dependence of ΔH [11, 12]. In Fig. 4, the IP ΔH is not a linear function of frequency, but possesses the “knee” behavior characteristic of the frequency dependence of linewidths dominated by the TMS mechanism. We have fit our data to the TMS model

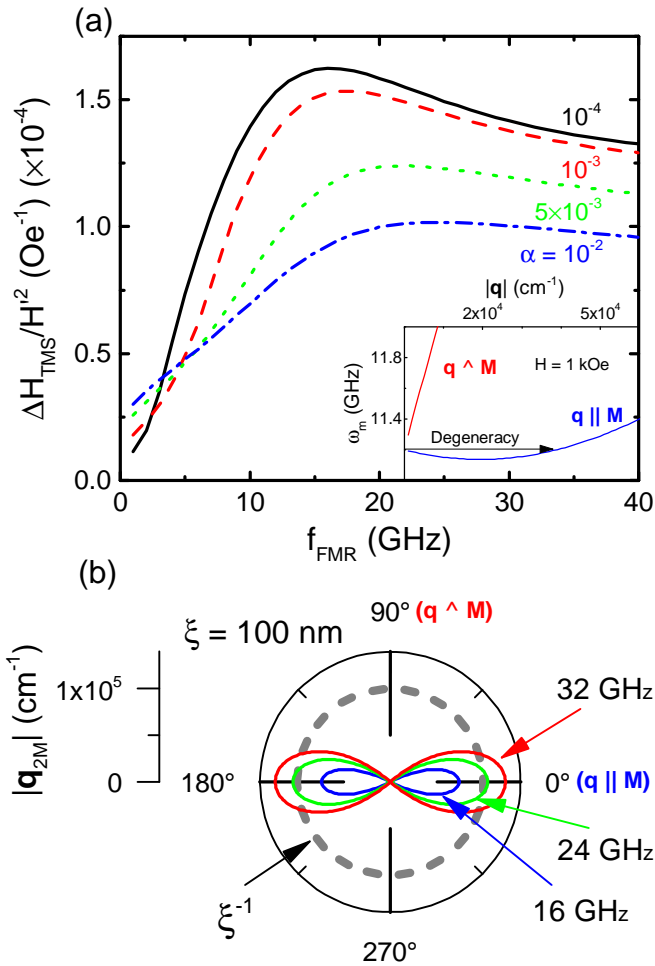


FIG. 5. (a) Two-magnon scattering linewidth contribution for values of Gilbert damping $\alpha = 10^{-2}, 5 \times 10^{-3}, 10^{-3}$, and 10^{-4} . The inset shows magnon dispersions for an applied field of $H = 1$ kOe. (b) Contours of the degenerate mode wavenumber q_{2M} in the film plane as a function of wavevector angle relative to the magnetization for $f_{FMR} = 16, 24$, and 32 GHz. The dashed circle indicates the wavenumber of a defect with size $\xi = 100$ nm.

described by McMichael and Krivosik [12], in which the TMS linewidth ΔH_{TMS} is given by [26, 27]

$$\Delta H_{TMS} = \frac{\gamma^2 \xi^2 H'^2}{df/dH|_{f_{FMR}}} \int \Gamma_{0q} C_q(\xi) \delta_\alpha(\omega - \omega_q) d^2 q, \quad (3)$$

where Γ_{0q} is the defect-mediated interaction term between magnons at wavevector 0 and q , $C_q(\xi) = (1 + (q\xi)^2)^{-3/2}$ is the correlation function of the magnetic system with correlation length ξ , and H' is the magnitude of the characteristic inhomogeneity (units of magnetic field). The δ_α -function in Eq. 3 selects out magnon scattering channels which conserve energy. In the limit of zero intrinsic damping it is identical to the Dirac delta function, but for finite α a Lorentzian function of width $\delta\omega = (2\alpha\omega/\gamma)d\omega/dH$ is used. The magnon dispersion

relation determining ω_q was taken as the usual Damon-Eshbach thin film result [26, 28] with the addition of magnetocrystalline anisotropy stiffness field terms extracted from the dependence of the resonance field on the applied frequency for the IP configuration. The IP FMR linewidth data shown in Fig. 4 were fit to Eq. 1 (with Eq. 3 used to evaluate ΔH_{TMS}) with ξ , α , and H' as fitting parameters. We indicate that some degree of uncertainty will result from this fitting procedure, because for linewidth data collected over a limited frequency range ξ and α cannot be independently constrained. We emphasize, however, that α is effectively determined by the PP measurement. In addition, we note that in Eq. 1 ΔH_0 is fixed (i.e. taken as isotropic) to the value given by the PP linewidth measurements shown in Fig. 2. Although certain realizations of inhomogeneity may result in an anisotropic ΔH_0 (see Ref. [14] for a good discussion), it is clear by inspection of Figs. 2 and 4 that nonzero values of ΔH_0 are needed to describe the data, and approaches beyond what we have described become intractable.

D. Effect of low intrinsic damping

The effect of low intrinsic damping on the two-magnon linewidth can be seen in Fig. 5(a). As α decreases, ΔH_{TMS} steadily increases and becomes increasingly non-linear (and eventually nonmonotonic) with frequency, all other parameters being fixed. In particular, a “knee” in the frequency dependence becomes more pronounced for low damping (see e.g. Fig. 5(a) curve for $\alpha = 10^{-4}$). The physics giving rise to the knee behavior is indicated in Fig. 5(b). The TMS process scatters magnons from zero to non-zero wavevector at small q . At the corresponding (large) length scales, there is presumed to be sufficient disorder to allow for the momentum q to be transferred to the magnon system. In the simplest case, there should be a length scale ξ below which the disorder decreases, so that the film becomes effectively more uniform at large wavevectors. The corresponding FMR frequencies are those for which the contours of constant frequency (the figure eights in Fig. 5) in q -space have extrema at $q \sim \xi^{-1}$. The TMS rate is also determined by the interplay of the magnon density of states, the effective area in q -space, and the Gilbert damping. The knee behavior is more pronounced for low α due to the increased weight of the van Hove singularity in the integrand of Eq. 3. The PP measurement has confirmed that all of these epitaxial Heusler films lie within the range $\alpha < 2 \times 10^{-3}$. We conclude that ferromagnetic films with ultralow α are increasingly prone to large TMS linewidths (particularly for metals with large M_s). In practice, this is why experimental reports [7, 22, 23] of ultralow α have almost all utilized the PP geometry.

TABLE II. Summary of the fitting parameters used to fit the in-plane data of Fig. 4 (black squares and red circles) to Eqs. 1 and 3.

Sample (Field Direction)	α ($\times 10^{-3}$)	ξ (nm)	H' (Oe)
CMS⟨110⟩	1.6 ± 0.2	28	91
CMS⟨100⟩	1.5 ± 0.1	28	50
CMA⟨110⟩	3.1 ± 0.2	55	61
CMA⟨100⟩	4.7 ± 0.4	64	170
CFA⟨110⟩	2.0 ± 0.3	18	83
CFA⟨100⟩	N/A	N/A	N/A

E. Discussion

The results of the IP linewidth fits to Eqs. 1 and 3 are summarized in Table II. In the case of CMS, the high-frequency slopes in Fig. 4(a) approach the same value along each direction, as would be expected when the frequency is large enough for the TMS wavevector to exceed the inverse of any defect correlation length and the Gilbert α is isotropic (within error limits).

Next, we discuss the CMA IP data shown in Fig. 4(b) and Table II. It is clear from this figure that a good fit can be obtained along both ⟨100⟩ and ⟨110⟩ directions. In Table II it can be seen that the value of the defect correlation length ξ is approximately the same along both directions. However, the values of α we obtain from fitting to Eqs. 1 and 3 do not agree well with the PP value of $\alpha_{001} = 1.8 \times 10^{-3}$ (Fig. 2). Anisotropic values of α have been both predicted [5, 10] and observed [29], and anisotropic α is possibly the explanation of our best-fit results. The in-plane ⟨100⟩ and ⟨001⟩ directions are equivalent in the bulk, so the anisotropy would necessarily be due to an interface anisotropy energy or tetragonal distortion due to strain.

Finally, we discuss the CFA linewidths shown in Fig. 4(c) and Table II. This sample has by far the largest two-magnon scattering contribution, which is likely related to the anomalously large inhomogeneous broadening and low intrinsic damping [see Fig. 5(a)] observed in the PP measurement. A good fit of the data was obtained when the field was applied along the ⟨110⟩ direction. Notably, the IP ⟨110⟩ best fit value of 2.1×10^{-3} is nearly a factor of 3 larger than the α_{001} upper bound on the same sample (Table I), strongly suggesting anisotropic Gilbert α . A striking anisotropy in the IP linewidth was revealed upon rotating the magnetization to the ⟨100⟩ orientation. For the ⟨100⟩ case, which yielded the largest TMS linewidths measured on this family of films, we were not able to fit the data to Eq. 3 using a set of physically reasonable input parameters. We believe that this is related to the consideration that higher order terms in the inhomogeneous magnetic energy (see Ref. [26]) need to be taken into account. Another reason why this may be the case is that the model of McMichael and Krivosik [12] assumes the inhomogeneities to be grain-like, whereas

atomic force microscopy images [see Fig. 1(d)] of these samples imply that grains, if they exist, are much larger than the defect correlation lengths listed in Table II, which are of order 10's of nm.

F. Summary and Conclusion

We conclude by discussing the successes and limitations of the McMichael and Krivosik [12] model in analyzing our Heusler film FMR linewidth data. We have shown that two-magnon scattering is the extrinsic linewidth-broadening mechanism in our samples. Any model which takes this as its starting point will predict much of the qualitative behavior we observe, such as the knee behavior and the large linewidths IP for low α films. The TMS model used in this article (for the purpose of separating TMS and Gilbert linewidth contributions) is likely only as accurate as its representation of the inhomogeneous magnetic field and the underlying assumption for the behavior of $C_q(\xi)$. Grain-like defects are assumed, which essentially give a random magnetocrystalline anisotropy field. Grains are clearly not the defect causing two-magnon scattering in our samples, which can be seen in the smoothness of our films [Fig. 1(d)]. Misfit dislocations, a much more likely candidate in our opinion, would cause an effective inhomogeneous magnetic field which could certainly have a more complicated spatial profile and lead to anisotropic two-magnon scattering (see Ref. [14]). The perturbative nature of the model also brings its own limitations, and we believe that the CFA⟨100⟩ data (for which we cannot obtain a satisfactory fit) is exemplary of a breakdown in the model for strong TMS. Future work should go into methods of treating the two-magnon scattering differently based on the type of crystalline defects present, which will in turn allow a more reliable extraction of the Gilbert damping α and facilitate the observation of anisotropic Gilbert damping, enabling quantitative comparison to first-principles calculations.

Regardless of the model limitations, we emphasize three critical observations drawn from the linewidth measurements presented in this article. First, in all cases we observe large and anisotropic TMS linewidth contributions, which imply inhomogeneity correlation length-scales of order tens-to-hundreds of nanometers. The microscopic origin of these inhomogeneities is the subject of ongoing work, but are likely caused by arrays of misfit dislocations [14]. The relatively large length-scale of these defects may cause them to be easily overlooked in epitaxial film characterization techniques such as XRD and HAADF-STEM, but still strongly influence magnetization dynamics. It is likely that these defects and their influence on the FMR linewidth through TMS have obscured confirmation of Kamberský's model for anisotropic and (in the case of Heusler compounds) ultralow intrinsic damping in metallic ferromagnets. Second, we observed low intrinsic damping through our PP measurement, which was $< 2 \times 10^{-3}$ for all of our sam-

plexes. Finally, we have presented the mechanism by which ultralow damping films are extraordinarily susceptible to large TMS FMR linewidths, the anisotropy of which may dominate, or conceal, underlying anisotropic Kambersky damping.

This work was supported by NSF under DMR-1708287 and by SMART, a center funded by nCORE, a Semi-

conductor Research Corporation program sponsored by NIST. The sample growth was supported by the DOE under DE-SC0014388 and the development of the growth process by the Vannevar Bush Faculty Fellowship (ONR N00014-15-1-2845). Parts of this work were carried out in the Characterization Facility, University of Minnesota, which receives partial support from NSF through the MRSEC program.

[1] V. Kamberský, On the Landau-Lifshitz relaxation in ferromagnetic metals, *Canadian Journal of Physics* **48**, 2906 (1970).

[2] V. Kamberský, On ferromagnetic resonance damping in metals, *Czechoslovak Journal of Physics* **26**, 1366 (1976).

[3] D. Steiauf and M. Fähnle, Damping of spin dynamics in nanostructures: An ab initio study, *Physical Review B* **72**, 064450 (2005).

[4] K. Gilmore, Y. U. Idzerda, and M. D. Stiles, Identification of the Dominant Precession-Damping Mechanism in Fe, Co, and Ni by First-Principles Calculations, *Physical Review Letters* **99**, 027204 (2007).

[5] K. Gilmore, M. D. Stiles, J. Seib, D. Steiauf, and M. Fähnle, Anisotropic damping of the magnetization dynamics in Ni, Co, and Fe, *Physical Review B* **81**, 174414 (2010).

[6] D. Ralph and M. Stiles, Spin transfer torques, *Journal of Magnetism and Magnetic Materials* **320**, 1190 (2008).

[7] M. A. W. Schoen, D. Thonig, M. L. Schneider, T. J. Silva, H. T. Nembach, O. Eriksson, O. Karis, and J. M. Shaw, Ultra-low magnetic damping of a metallic ferromagnet, *Nature Physics* **12**, 839 (2016).

[8] S. Mankovsky, D. Ködderitzsch, G. Woltersdorf, and H. Ebert, First-principles calculation of the Gilbert damping parameter via the linear response formalism with application to magnetic transition metals and alloys, *Physical Review B* **87**, 014430 (2013).

[9] C. Liu, C. K. A. Mewes, M. Chshiev, T. Mewes, and W. H. Butler, Origin of low Gilbert damping in half metals, *Applied Physics Letters* **95**, 022509 (2009).

[10] T. Qu and R. H. Victora, Dependence of Kambersky damping on Fermi level and spin orientation, *Journal of Applied Physics* **115**, 17C506 (2014).

[11] R. Arias and D. L. Mills, Extrinsic contributions to the ferromagnetic resonance response of ultrathin films, *Physical Review B* **60**, 7395 (1999).

[12] R. McMichael and P. Krivosik, Classical Model of Extrinsic Ferromagnetic Resonance Linewidth in Ultrathin Films, *IEEE Transactions on Magnetics* **40**, 2 (2004).

[13] M. A. W. Schoen, J. M. Shaw, H. T. Nembach, M. Weiler, and T. J. Silva, Radiative damping in waveguide-based ferromagnetic resonance measured via analysis of perpendicular standing spin waves in sputtered permalloy films, *Physical Review B* **92**, 184417 (2015).

[14] G. Woltersdorf and B. Heinrich, Two-magnon scattering in a self-assembled nanoscale network of misfit dislocations, *Physical Review B* **69**, 184417 (2004).

[15] S. Mizukami, D. Watanabe, M. Oogane, Y. Ando, Y. Miura, M. Shirai, and T. Miyazaki, Low damping constant for Co₂FeAl Heusler alloy films and its correlation with density of states, *Journal of Applied Physics* **105**, 07D306 (2009).

[16] S.-Z. Qiao, Q.-N. Ren, R.-R. Hao, H. Zhong, Y. Kang, S.-S. Kang, Y.-F. Qin, S.-Y. Yu, G.-B. Han, S.-S. Yan, and L.-M. Mei, Broad-Band FMR Linewidth of Co₂MnSi Thin Films with Low Damping Factor: The Role of Two-Magnon Scattering, *Chinese Physics Letters* **33**, 047601 (2016).

[17] Y. Cui, J. Lu, S. Schäfer, B. Khodadadi, T. Mewes, M. Osofsky, and S. A. Wolf, Magnetic damping and spin polarization of highly ordered B2 Co₂FeAl thin films, *Journal of Applied Physics* **116**, 073902 (2014).

[18] S. S. Kalarickal, P. Krivosik, M. Wu, C. E. Patton, M. L. Schneider, P. Kabos, T. J. Silva, and J. P. Nibarger, Ferromagnetic resonance linewidth in metallic thin films: Comparison of measurement methods, *Journal of Applied Physics* **99**, 093909 (2006).

[19] E. Montoya, T. McKinnon, A. Zamani, E. Girt, and B. Heinrich, Broadband ferromagnetic resonance system and methods for ultrathin magnetic films, *Journal of Magnetism and Magnetic Materials* **356**, 12 (2014).

[20] C. Kittel, On the Theory of Ferromagnetic Resonance Absorption, *Physical Review* **73**, 155 (1948).

[21] A. Kumar, F. Pan, S. Husain, S. Akansel, R. Brucas, L. Bergqvist, S. Chaudhary, and P. Svedlindh, Temperature-dependent Gilbert damping of Co₂FeAl thin films with different degree of atomic order, *Physical Review B* **96**, 224425 (2017).

[22] M. Oogane, A. P. McFadden, K. Fukuda, M. Tsunoda, Y. Ando, and C. J. Palmstrøm, Low magnetic damping and large negative anisotropic magnetoresistance in half-metallic Co_{2-x}Mn_{1+x}Si Heusler alloy films grown by molecular beam epitaxy, *Applied Physics Letters* **112**, 262407 (2018).

[23] C. Guillemand, S. Petit-Watelot, L. Pasquier, D. Pierre, J. Ghanbaja, J.-C. Rojas-Sánchez, A. Bataille, J. Rault, P. Le Fèvre, F. Bertran, and S. Andrieu, Ultralow Magnetic Damping in Co₂Mn-Based Heusler Compounds: Promising Materials for Spintronics, *Physical Review Applied* **11**, 064009 (2019).

[24] K. Zakeri, J. Lindner, I. Barsukov, R. Meckenstock, M. Farle, U. von Hörsten, H. Wende, W. Keune, J. Rocker, S. S. Kalarickal, K. Lenz, W. Kuch, K. Baberschke, and Z. Frait, Spin dynamics in ferromagnets: Gilbert damping and two-magnon scattering, *Physical Review B* **76**, 104416 (2007).

[25] H. Kurebayashi, T. D. Skinner, K. Khazen, K. Olejník, D. Fang, C. Ciccarelli, R. P. Campion, B. L. Gallagher, L. Fleet, A. Hirohata, and A. J. Ferguson, Uniaxial anisotropy of two-magnon scattering in an ultrathin epitaxial Fe layer on GaAs, *Applied Physics Letters* **102**, 062415 (2013).

- [26] P. Krivosik, N. Mo, S. Kalarickal, and C. E. Patton, Hamiltonian formalism for two magnon scattering microwave relaxation: Theory and applications, *Journal of Applied Physics* **101**, 083901 (2007).
- [27] S. S. Kalarickal, P. Krivosik, J. Das, K. S. Kim, and C. E. Patton, Microwave damping in polycrystalline Fe-Ti-N films: Physical mechanisms and correlations with composition and structure, *Physical Review B* **77**, 054427 (2008).
- [28] J. R. Eshbach and R. W. Damon, Surface Magnetostatic Modes and Surface Spin Waves, *Physical Review* **118**, 1208 (1960).
- [29] L. Chen, S. Mankovsky, S. Wimmer, M. A. W. Schoen, H. S. Körner, M. Kronseder, D. Schuh, D. Bougeard, H. Ebert, D. Weiss, and C. H. Back, Emergence of anisotropic Gilbert damping in ultrathin Fe layers on GaAs(001), *Nature Physics* **14**, 490 (2018).